Supporting information

The role of the Li^+ node in the Li-BH_4 substructure of double-cation tetrahydroborates

Authors

Pascal Schouwink[a], L'ubomír Smrčok[b] and Radovan Černý[a]*

[a]Department of Quantum Matter Physics, Laboratory of Crystallography, University of Geneva, Quai Ernest-Ansermet 24, Geneva, 1211, Switzerland

[b]Institute of Inorganic Chemistry, Slovak Academy of Sciences, Dúbravská cesta 9, Bratislava, 845 36, Slovak Republic

Correspondence email: Radovan.Cerny@unige.ch

Table S1 Different samples with compositions $LiBH_4$: ABH_4 listed in column 1 and the contained phases in column 2. The temperature range where the respective phase is observed is given in column 3, the last column summarizes the general topology of the Li-BH_4 substructure.

Sample	Compound	Stability interval [K]	Li-BH_4 connectivity
LiRb_11	*m*-$LiRb(BH_4)_2$	RT-403	chain of double -rings
LiRb_11	*o*-$LiRb(BH_4)_2$	403-414	sheet
LiRb_21	*h*-$Li_2Rb(BH_4)_3$	RT-392	framework
LiCs_11 **LiCs_21**	*o*-$LiCs(BH_4)_2$	RT-430	sheet
LiCs_21	*h*-$Li_2Cs(BH_4)_3$	RT-420	framework
LiCs_11 **LiCs_21**	*m*-$Li_2Cs(BH_4)_3$	RT-331	sheet
LiCs_11	*m*-$LiCs_2(BH_4)_3$	RT-450	vertex sharing chain
LiCs_11 **LiCs_21**	*o*-$Li_3Cs_2(BH_4)_5$	345-430	sheet
LiCs_11	*m*-$Li_2Cs_3(BH_4)_5$	RT-345	vertex-edge-sharing chain
LiCs_31 **LiCs_41**	*m*-$Li_3Cs(BH_4)_4$	RT-398	framework

Table S2 Experimental Table 1

	h-$Li_2Cs(BH_4)_3$	*h*-$Li_2Rb(BH_4)_3$	*m*-$Li_3Cs(BH_4)_4$	*m*-$Li_2Cs(BH_4)_3$	*m*-$Li_2Cs_3(BH_4)_5$
Crystal data					
Chemical formula	$B_3CsH_{12}Li_2$	$B_3H_{12}Li_2Rb$	$B_4CsH_{16}Li_3$	$B_3CsH_{12}Li_2$	$B_5Cs_3H_{20}Li_2$
M_r	191.32	143.88	213.10	191.32	486.81
Crystal system, space group	Hexagonal, $P6_222$	Hexagonal, $P6_222$	Monoclinic, $P2_1/c$	Monoclinic, Cc	Monoclinic, $P2_1/c$
Temperature (K)	384	300	293	293	293
a, *b*, *c* (Å) *β*	7.6634 (4), 7.6634 (4), 12.1279 (7)	7.474 (2), 7.474 (2), 11.585 (3)	8.1992 (3), 12.3044 (5), 11.9009 (5) 123.767 (2)	7.574 (2), 7.948 (2), 12.880 (3) 89.97 (1)	14.444 (1), 7.4218 (6), 14.7907 (10) 104.470 (3)
V (Å^3)	616.8 (1)	560.4 (3)	998.1 (1)	775.4 (3)	1535.3 (2)
Z	3	3	4	4	4
Radiation type	Synchrotron, λ = 0.826887 Å	Synchrotron, λ = 0.826887 Å	Synchrotron, λ = 0.82103 Å	Synchrotron, λ = 0.826887 Å	Synchrotron, λ = 0.826887 Å
Data collection					
Diffractometer	Two-axis goniometer diffractometer	Two-axis goniometer diffractometer	Two-axis goniometer diffractometer	Two-axis goniometer diffractometer	Two-axis goniometer diffractometer
Specimen mounting	Capillary	Capillary	Capillary	Capillary	Capillary
Data collection mode	Transmission	Transmission	Transmission	Transmission	Transmission
Scan method	Stationary detector	Stationary detector	Stationary detector	Stationary detector	Stationary detector
2θ values (°)	3.6-30	3.6-30	2-57	3.6-30	3.6-30
Refinement					
R factors and goodness of fit No. of data points	R_p = 0.045, R_{wp} = 0.036, R_{exp} = 0.011, R_{Bragg} = 0.043, χ^2 = 10.890 7029	R_p = 0.018, R_{wp} = 0.023, R_{exp} = 0.010, R_{Bragg} = 0.015, χ^2 = 4.709 7029	R_p = 0.025, R_{wp} = 0.018, R_{exp} = 0.001, R_{Bragg} = 0.019, χ^2 = 478.734 4855	R_p = 0.057, R_{wp} = 0.065, R_{exp} = 0.011, R_{Bragg} = 0.072, χ^2 = 34.340 7029	R_p = 0.105, R_{wp} = 0.108, R_{exp} = 0.011, R_{Bragg} = 0.078, χ^2 = 86.118 7029
No. of parameters	101	68	112	37	96
No. of constraints	10	10	19	18	26
No. of restraints	4	4	5	7	6
H-atom treatment	Rigid body BH_4	Rigid body BH_4	Rigid body BH_4	Rigid body BH_4	Rigid body BH_4

Table S3 Experimental Table 2.

	m-$LiCs_2(BH_4)_3$	*m*-$LiRb(BH_4)_2$	*o*-$Li_3Cs_2(BH_4)_5$	*o*-$LiCs(BH_4)_2$	*o*-$LiRb(BH_4)_2$
Crystal data					
Chemical formula	$B_3Cs_2H_{12}Li$	B_2H_8LiRb	$B_5Cs_2H_{20}Li_3$	B_2CsH_8Li	B_2H_8LiRb
M_r	317.28	122.09	360.85	169.53	122.09
Crystal system, space group	Monoclinic, *C*2/*c*	Monoclinic, *C*2/*m*	Orthorhombic, *Fddd*	Orthorhombic, $Cmc2_1$	Orthorhombic, $Cmc2_1$
Temperature (K)	368	296	384	368	411
a, *b*, *c* (Å)	7.6021 (11), 15.160 (2), 17.243 (2)	23.5931 (4), 4.6178 (7), 17.1893 (3)	13.5838 (8), 17.3001 (11), 23.9151 (15)	4.6817 (7), 15.950 (3), 7.9438 (13)	4.5711 (10), 15.4847 (10), 7.9355 (6)
β	92.693 (1)	97.776 (1)			
V (Å^3)	1985.0 (5)	1855.5 (3)	5620.1 (6)	593.2 (2)	561.69 (13)
Z	8	14	16	4	4
Radiation type	Synchrotron, λ = 0.826887 Å	Synchrotron, λ = 0.82257 Å	Synchrotron, λ = 0.826887 Å	Synchrotron, λ = 0.82711 Å	Synchrotron, λ = 0.82257 Å
Data collection					
Diffractometer	Two-axis goniometer diffractometer	Two-axis goniometer diffractometer	Two-axis goniometer diffractometer	Two-axis goniometer diffractometer	Two-axis goniometer diffractometer
Specimen mounting	Capillary	Capillary	Capillary	Capillary	Capillary
Data collection mode	Transmission	Transmission	Transmission	Transmission	Transmission
Scan method	Stationary detector	Stationary detector	Stationary detector	Stationary detector	Stationary detector
2θ values (°)	3.6-30	1.5-35.5	3.6-30	3.6-30	1.5-35.5
Refinement					
R factors and goodness of fit	R_p = 0.032, R_{wp} = 0.042, R_{exp} = 0.011, R_{Bragg} = 0.024, χ^2 = 16.646	R_p = 0.022, R_{wp} = 0.035, R_{exp} = 0.001, R_{Bragg} = 0.017, χ^2 = 727.381	R_p = 0.045, R_{wp} = 0.036, R_{exp} = 0.011, R_{Bragg} = 0.048, χ^2 = 10.890	R_p = 0.033, R_{wp} = 0.045, R_{exp} = 0.011, R_{Bragg} = 0.072, χ^2 = 16.646	R_p = 0.031, R_{wp} = 0.072, R_{exp} = 0.001, R_{Bragg} = 0.086, χ^2 = 2498.000
No. of data points	7029	4054	7029	7029	4054
No. of parameters	138	103	101	138	48
No. of constraints	15	36	17	11	11
No. of restraints	3	7	4	4	1
H-atom treatment	Rigid body BH_4	Rigid body BH_4	Rigid body BH_4	Rigid body BH_4	Rigid body BH_4

Figure S1 Heating T-ramp 393-424 K (60 K/h, SNBL) of the sample LiRb_11 showing the phase transition from monoclinic to orthorhombic phase of $LiRb(BH_4)_2$ at 403 K and melting of the orthorhombic phase at 414 K.

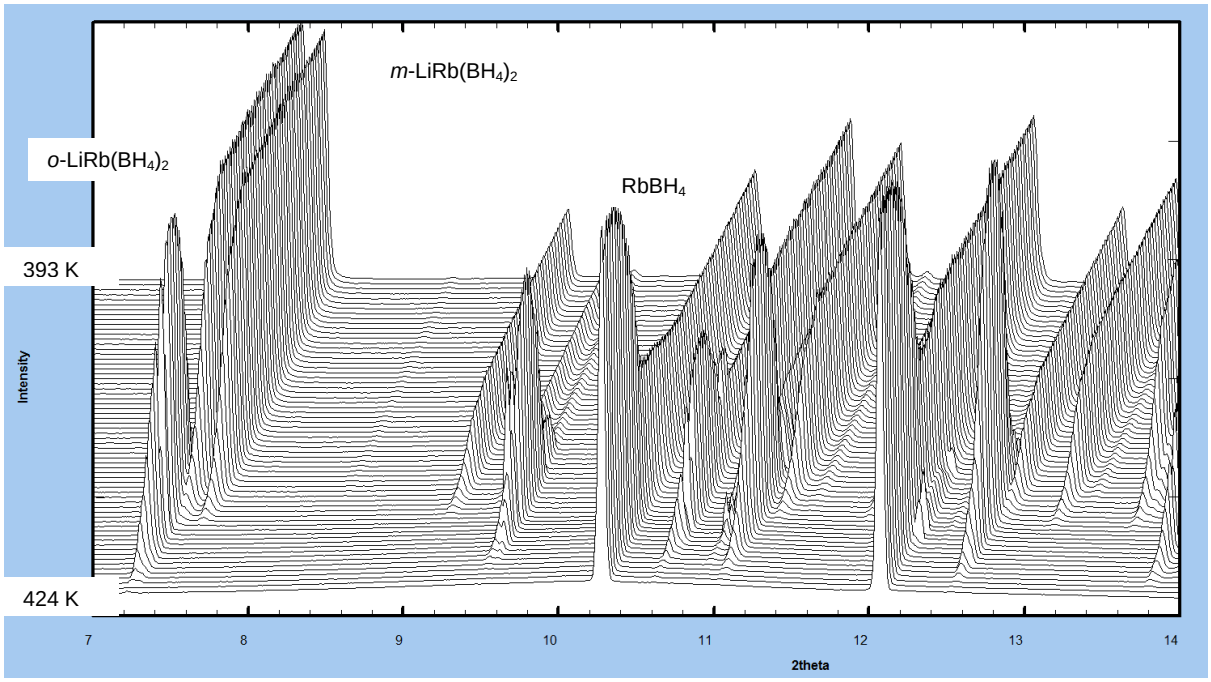

Figure S2 Cooling T-ramp 415-354 K (60 K/h, SNBL) of the sample LiRb_11 showing the crystallization of *o*-$LiRb(BH_4)_2$ at 409 K and the phase transition from the orthorhombic to monoclinic phase of $LiRb(BH_4)_2$ at 375 K. Note the irregular variation of powder peak intensities caused by grainy sample which has crystallized from the melt.

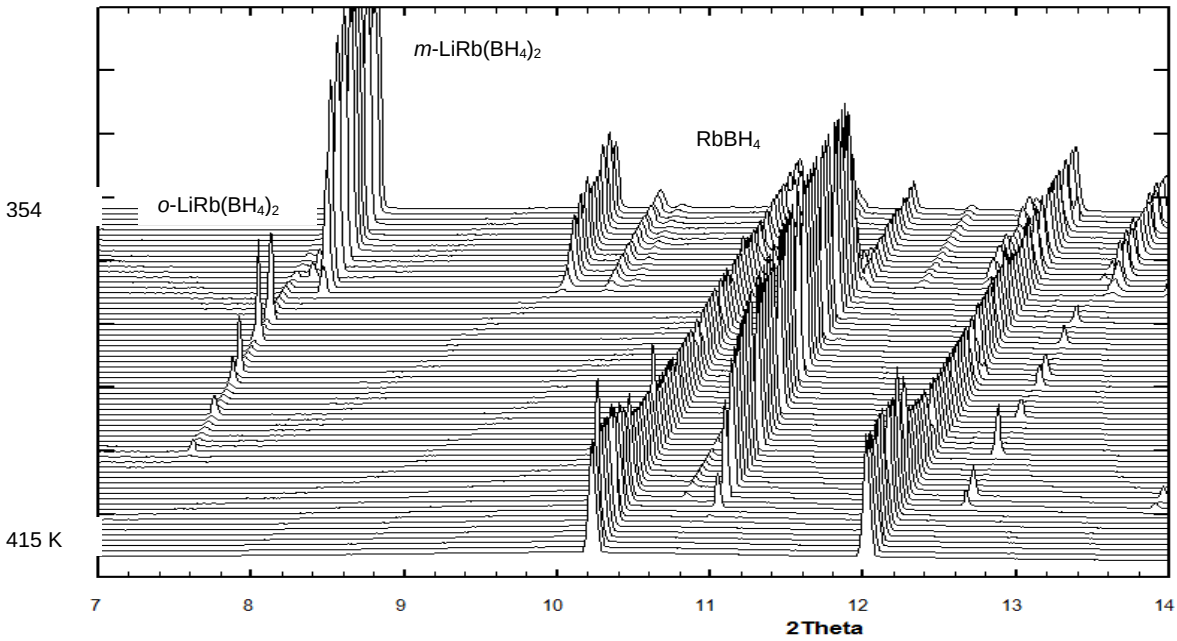

Figure S3 Three types of Li coordination observed in novel bi-alkali metal borohydrides. The interatomic distances in Å and bond angles are calculated from the DFT optimized structures with fixed lattice parameters. The standard uncertainties of the distances and angles are calculated from standard uncertainties of lattice parameters from Rietveld refinement and are on fourth and third decimal place, respectively. Li in blue, B in red, H in grey.

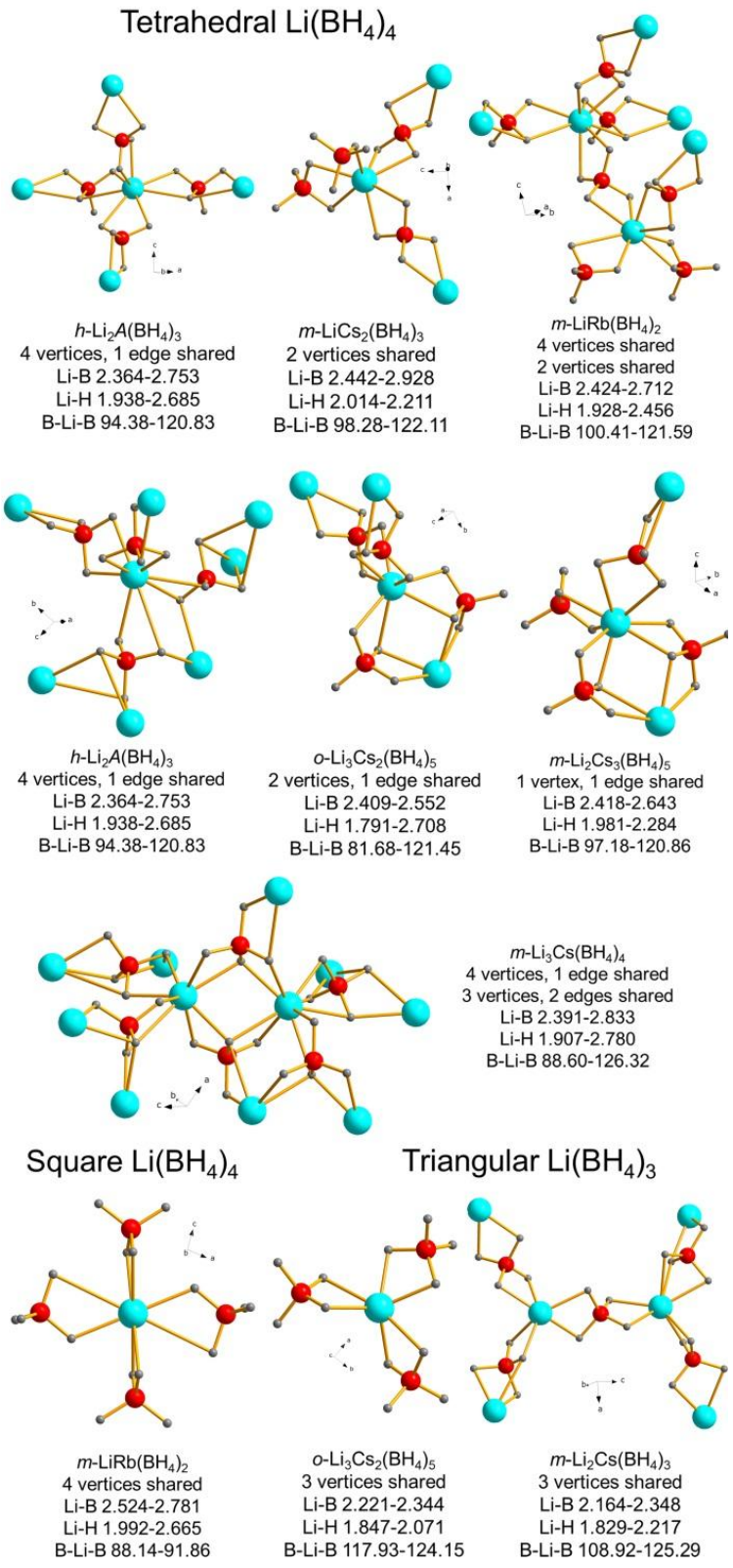

Figure S4 Rietveld plot (program TOPAS) for the SNBL data of the sample LiRb_11 measured at *RT*, using 0.8226 Å wavelength. Bragg peaks positions from top to the bottom: *m*-$LiRb(BH_4)_2$, $RbBH_4$, $NaBH_4$. The refined phase composition is given in wt. %. $R_{wp(bgr.\ corr.)} = 0.078$, $\chi^2 = 583$.

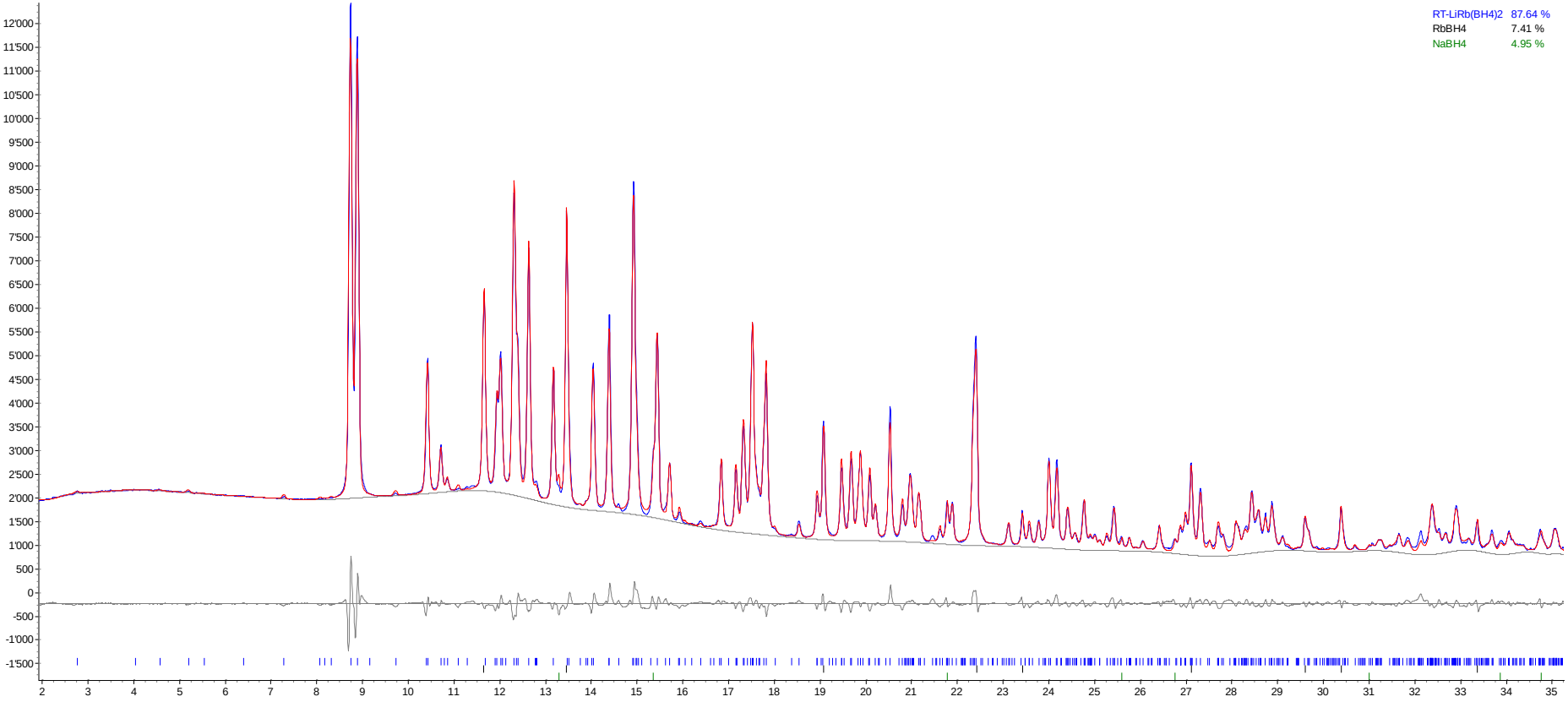

Figure S5 Rietveld plot (program TOPAS) for the SNBL data of the sample LiRb_11 measured at 411 K, using 0.8226 Å wavelength. Bragg peaks positions from top to the bottom: *o*-$LiRb(BH_4)_2$, $RbBH_4$, $NaBH_4$. The refined phase composition is given in wt. %. $R_{wp(bgr.\ corr.)} = 0.221$, $\chi^2 = 2484$.

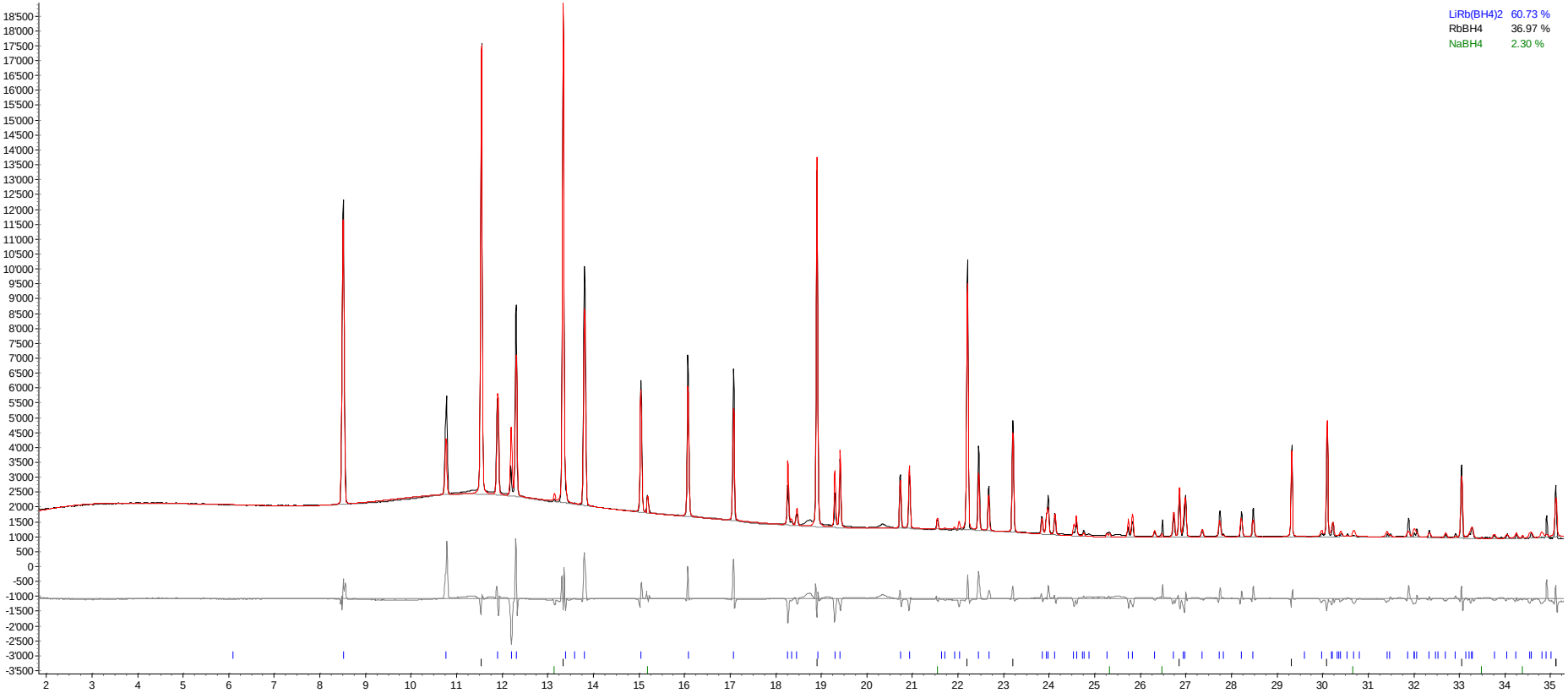

Figure S6 Rietveld plot (program TOPAS) for the SLS data of the sample LiRb_21 measured at *RT*, using 0.8271 Å wavelength. Bragg peaks positions from top to the bottom: *h*-$Li_2Rb(BH_4)_3$, *m*-$LiRb(BH_4)_2$, $NaBH_4$. The refined phase composition is given in wt. %. $R_{wp(bgr.\ corr.)} = 0.109$, $\chi^2 = 4$.

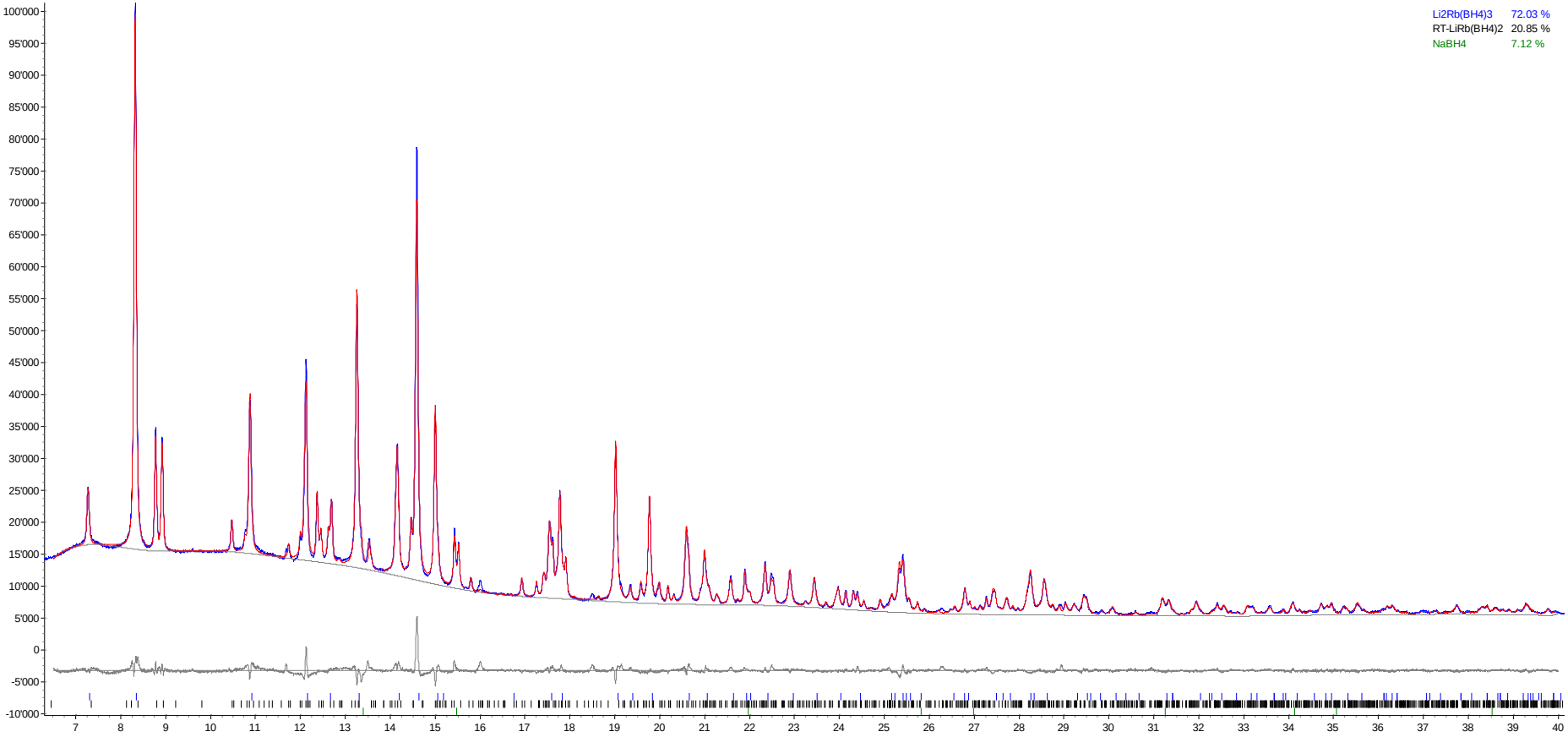

Figure S7 Heating-cooling T-ramp 293-473-293 K (60 K/h, SLS) of the sample LiCs_11showing *m*-$Li_2Cs_3(BH_4)_5$, *o*-$LiCs(BH_4)_2$, *m*-$Li_2Cs(BH_4)_3$ and unidentified impurity in as milled sample. While *m*-$Li_2Cs(BH_4)_3$ disappears already at 331 K, *m*-$Li_2Cs_3(BH_4)_5$ and impurity disappear, and phases *o*-$Li_3Cs_2(BH_4)_5$ and *m*-$LiCs_2(BH_4)_3$ appear simultaneously at 345 K. While *o*-$LiCs(BH_4)_2$ and *o*-$Li_3Cs_2(BH_4)_5$ disappear at 430 K, *m*-$LiCs_2(BH_4)_3$ melts at 450 K, recrystallizes on cooling and is stable at *RT*. Peaks of the unidentified impurity presented already in as milled sample are not labeled. Note the irregular variation of powder peak intensities caused by grainy sample started from 410 K.

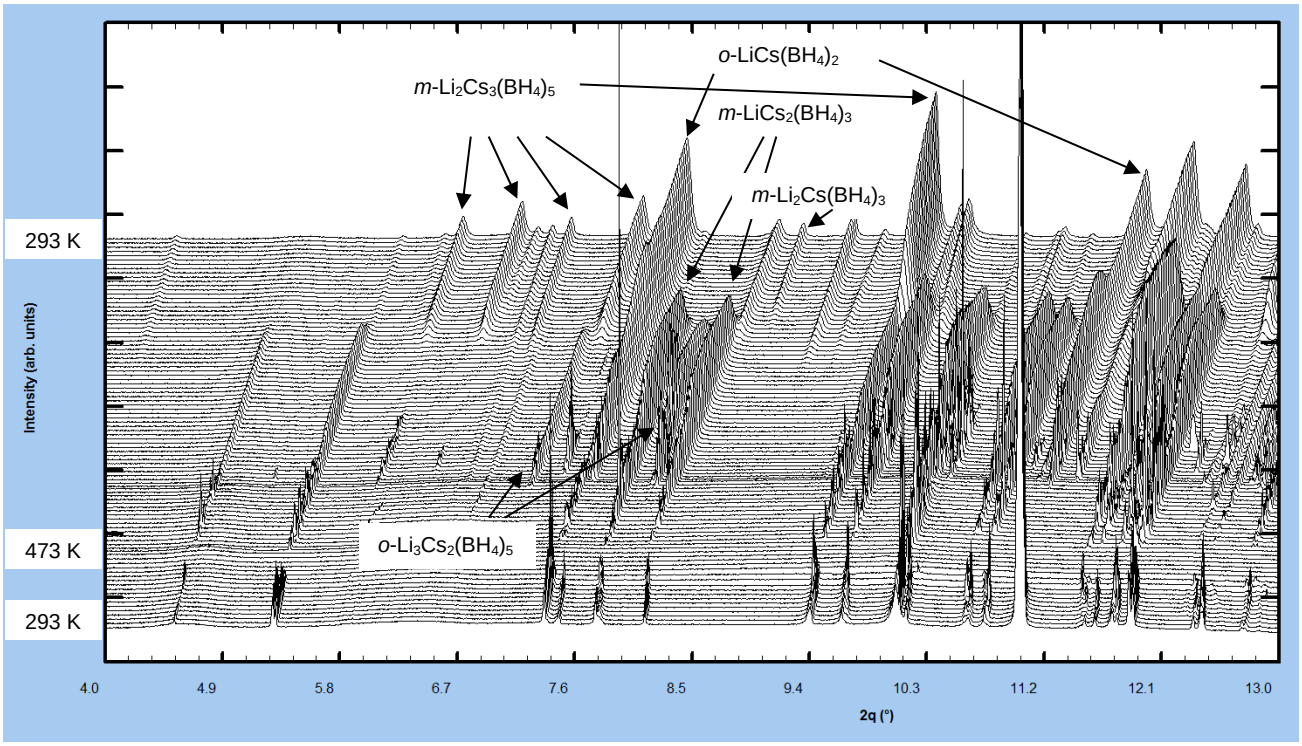

Figure S8 Heating-cooling T-ramp 293-430-293 K (60 K/h, SLS) of the sample LiCs_21 showing *m*-$Li_2Cs(BH_4)_3$ in as milled sample, its transformation on heating to *h*-$Li_2Cs(BH_4)_3$ at 348 K together with appearing of *o*-$LiCs(BH_4)_2$ and *o*-$Li_3Cs_2(BH_4)_5$. While *o*-$LiCs(BH_4)_2$ disappears at 397 K, the other two phases melt at 407 K. On cooling only *h*-$Li_2Cs(BH_4)_3$ recrystallizes and is stable at *RT*. Peaks of the unidentified impurity presented already in as milled sample and disappearing at 348 K are not labelled.

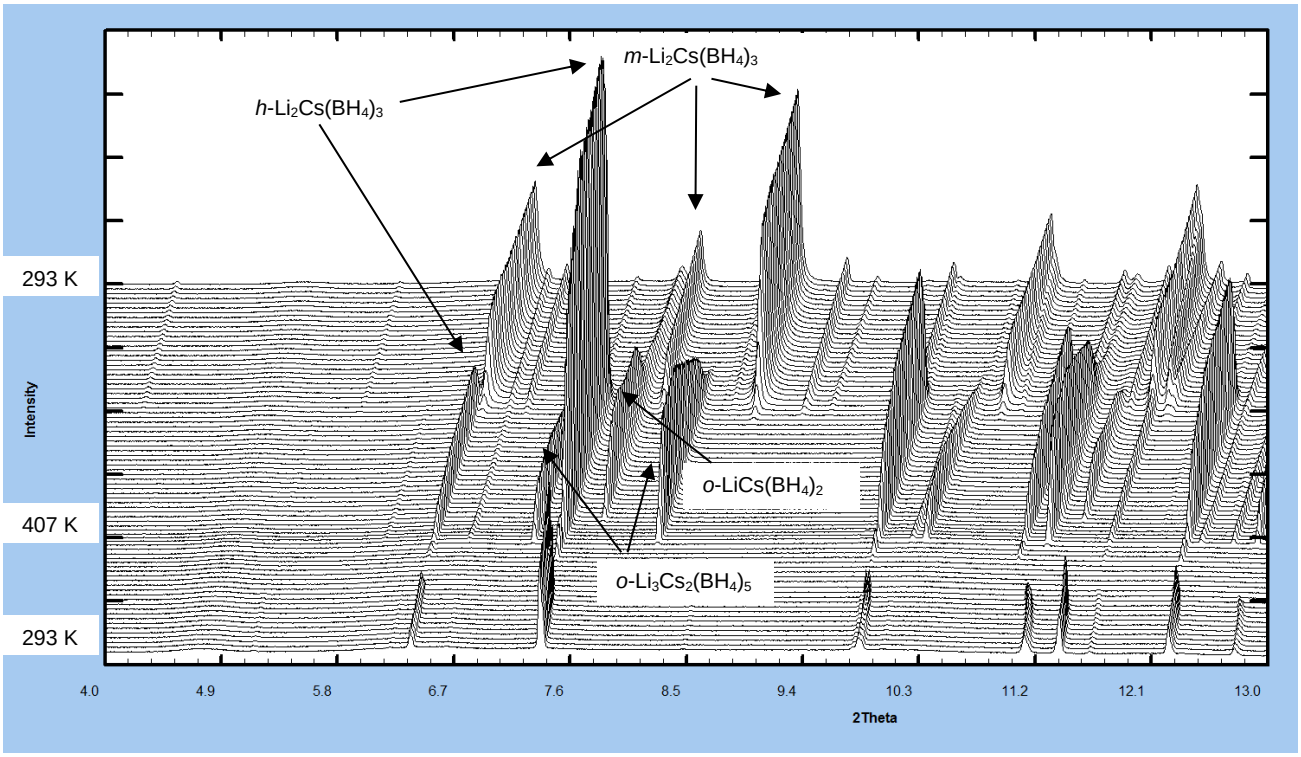

Figure S9 Rietveld plot (program TOPAS) for the SLS data of the sample LiCs_11 measured at *RT*, using 0.8271 Å wavelength. Bragg peaks positions from top to the bottom: *m*-$Li_2Cs(BH_4)_3$, *m*-$Li_2Cs_3(BH_4)_5$, *o*-$LiCs(BH_4)_2$. Peaks of the unidentified impurity are not labelled, and regions of the powder pattern containing only those peaks were excluded from the refinement. $R_{wp(bgr.\ corr.)} = 0.38$, $\chi^2 = 86$.

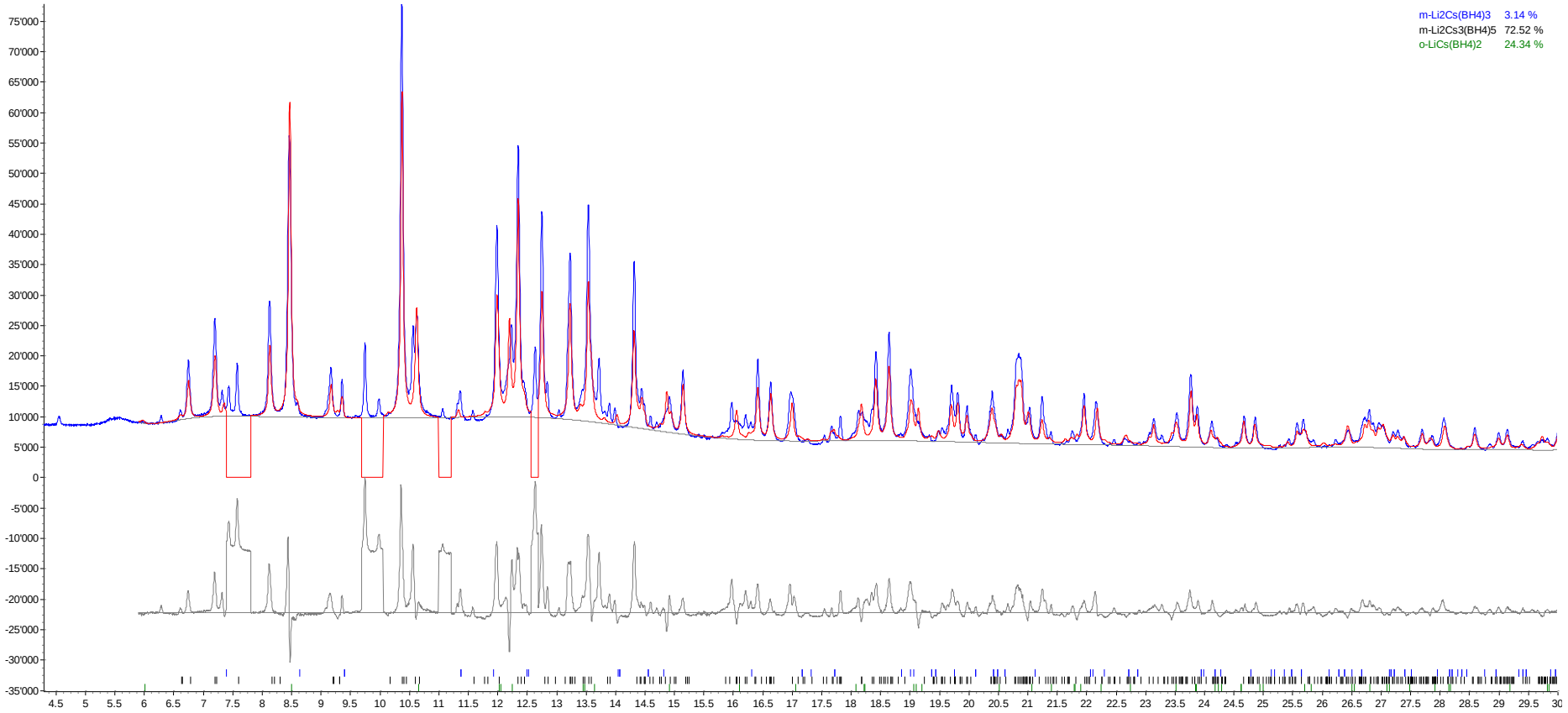

Figure S10 Rietveld plot (program TOPAS) for the SLS data of the sample LiCs_11 measured at 368 K, using 0.8271 Å wavelength. Bragg peaks positions from top to the bottom: *m*-$LiCs_2(BH_4)_3$, *o*-$Li_3Cs_2(BH_4)_5$, *o*-$LiCs(BH_4)_2$. $R_{wp(bgr.\ corr.)} = 0.174$, $\chi^2 = 16.61$.

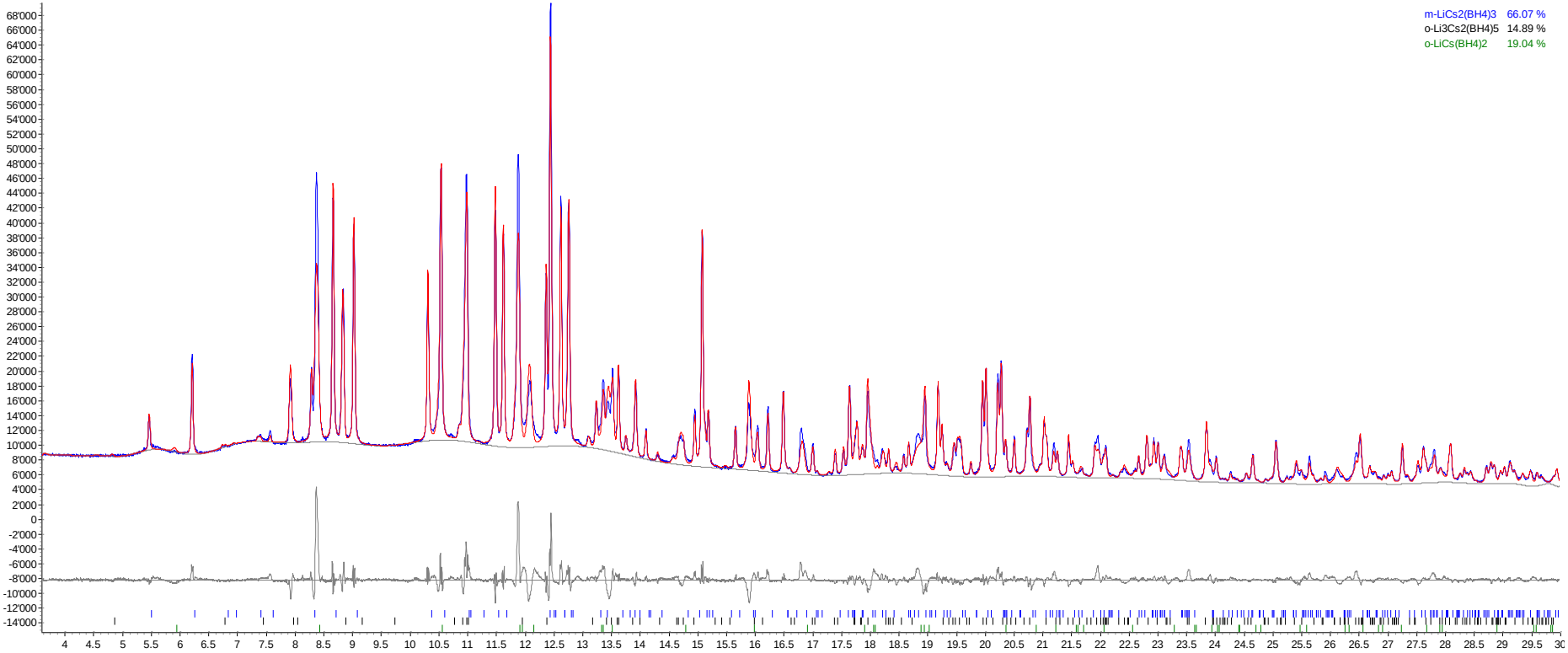

Figure S11 Rietveld plot (program TOPAS) for the SLS data of the sample LiCs_21 measured at RT, using 0.8271 Å wavelength. Bragg peaks positions for m-Li2Cs(BH4)3. Peaks of the unidentified impurity are not labelled, and regions of the powder pattern containing only those peaks were excluded from the refinement. $R_{wp(bgr.\ corr.)}$ = 0.186, $\chi 2$ = 34.34.

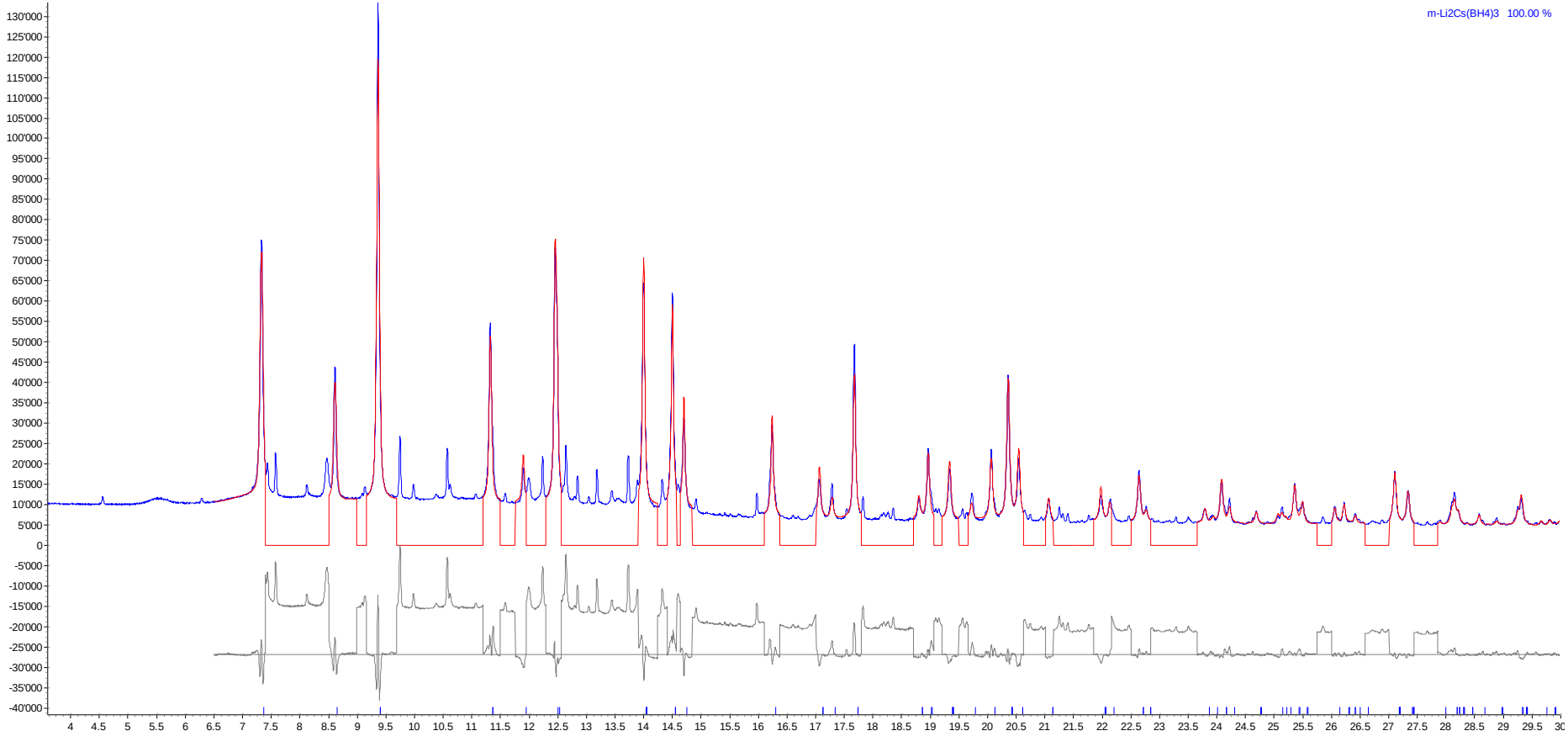

Figure S12 Rietveld plot (program TOPAS) for the SLS data of the sample LiCs_21 measured at 384 K, using 0.8271 Å wavelength. Bragg peaks positions from top to the bottom: *o*-$Li_3Cs_2(BH_4)_5$, *h*-$Li_2Cs(BH_4)_3$, *o*-$LiCs(BH_4)_2$. $R_{wp(bgr.\ corr.)} = 0.158$, $\chi^2 = 9.24$.

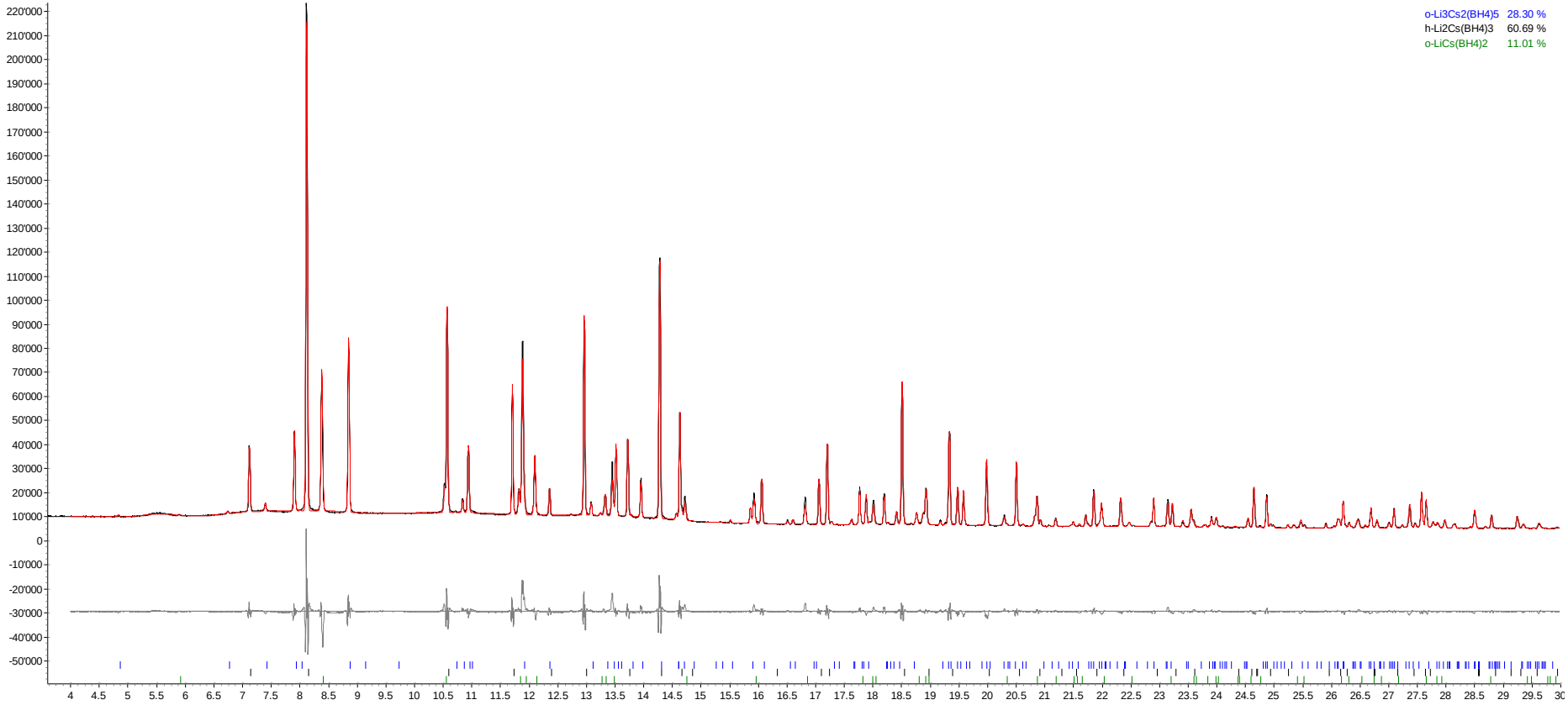

Figure S13 Heating-cooling T-ramp 293-473-293 K (180 K/h, SNBL) of the sample LiCs_31 showing *m*-$Li_3Cs(BH_4)_4$ and *m*-$Li_2Cs(BH_4)_3$ in as milled sample. While *m*-$Li_2Cs(BH_4)_3$ transforms at 345 K to *h*-$Li_2Cs(BH_4)_3$, *m*-$Li_3Cs(BH_4)_5$ disappears at 398 K. At 420 K *h*-$Li_2Cs(BH_4)_3$, melts, and recrystallizes on cooling at 410 K and is stable down to *RT*.

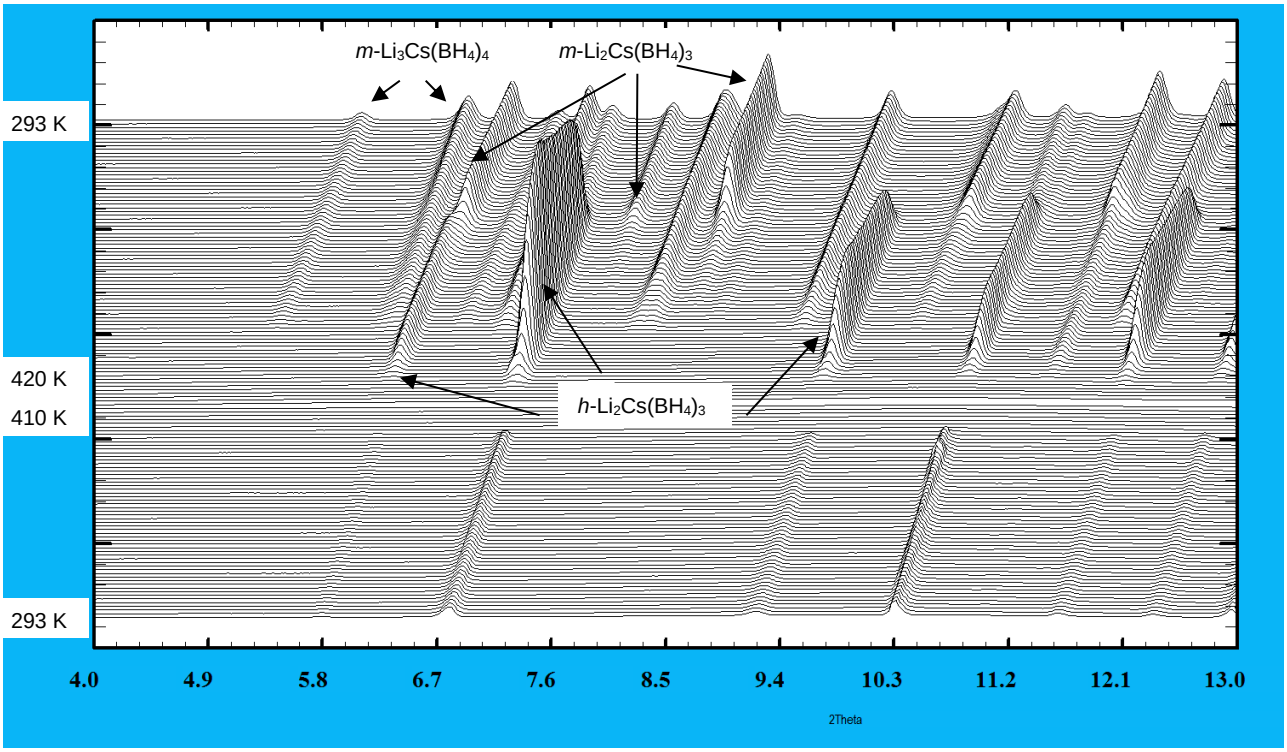

Figure S14 Rietveld plot (program TOPAS) for the SNBL data of the sample LiCs_31 measured at RT, using 0.8210 Å wavelength. Bragg peaks positions from top to the bottom: m-Li2Cs(BH4)4, m-Li3Cs(BH4)3. $R_{wp(bgr.\ corr.)}$ = 0.066, $\chi 2$ = 478.

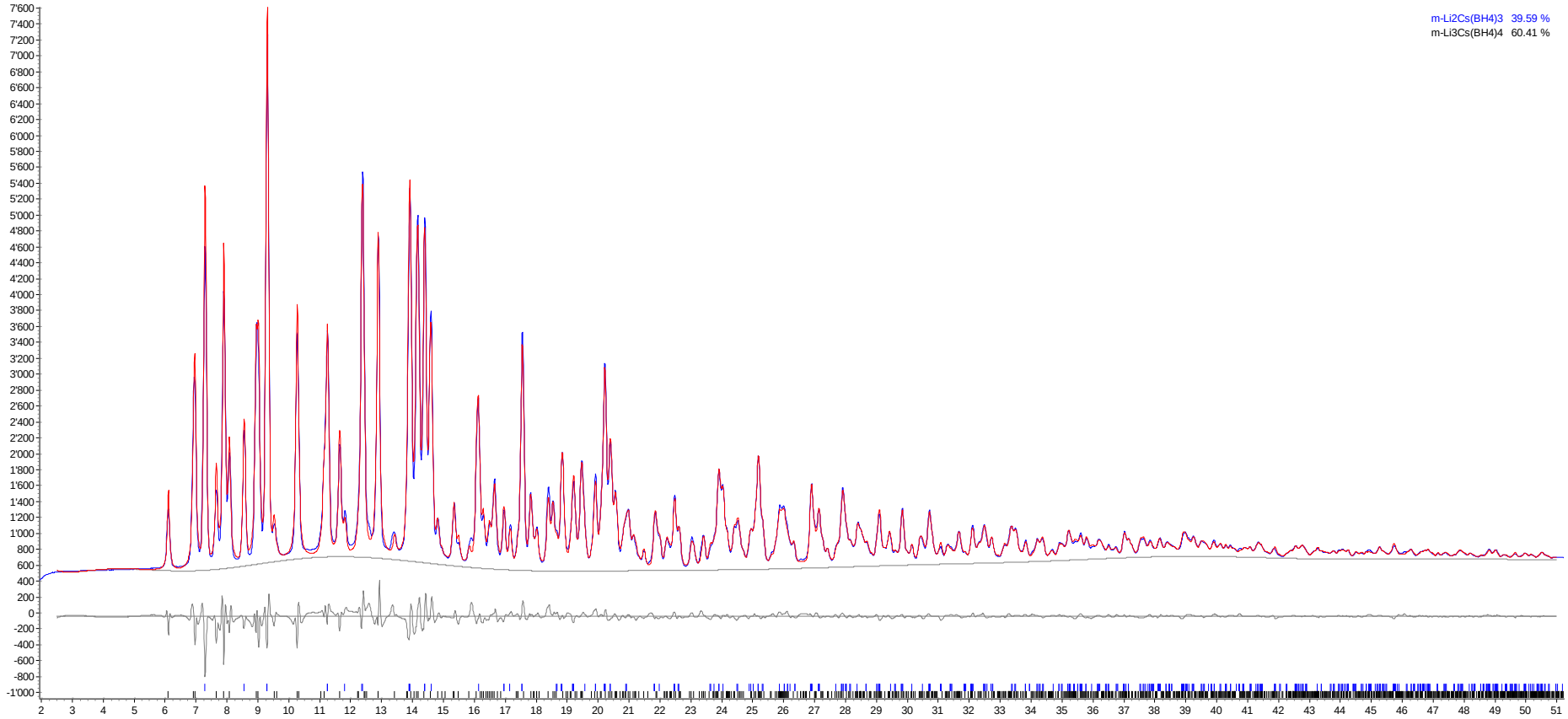

Figure S15 In-situ ball-milling performed at ID15A of ESRF, showing the phase evolution as a function of milling time (0 minutes: top of image), milling was performed at 20 Hz.

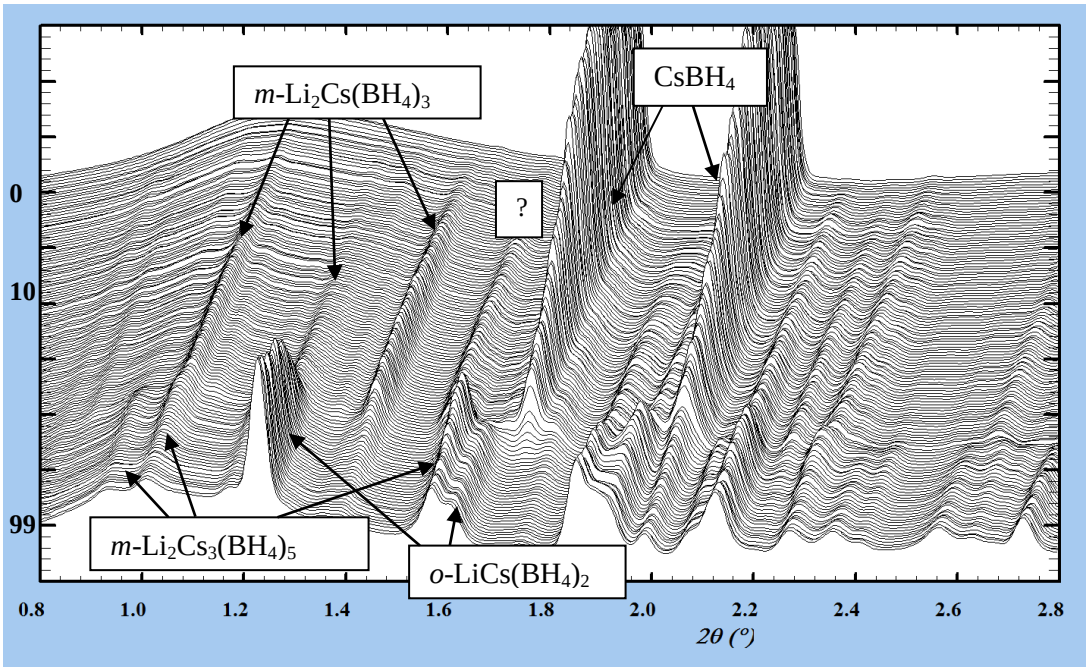

Figure S16 Hexagonal 2 : 1 phases as BH_4 filled $CrSi_2$ structure type are shown on *h*-$Li_2Cs(BH_4)_3$ example.